

1 **Hydrogen radicals-induced electrocatalytic N₂ reduction at low potential**

2 Xueting Feng^{1,5}, Jiyuan Liu^{2,5}, Long Chen³, Ya Kong¹, Zedong Zhang⁴, Zixuan Zhang¹,
3 Dingsheng Wang⁴, Wen Liu³, Shuzhou Li^{2,*}, Lianming Tong^{1,*}, Jin Zhang^{1,*}

4 ¹Center for Nanochemistry, Beijing Science and Engineering Center for Nanocarbons,
5 Beijing National Laboratory for Molecular Sciences, College of Chemistry and
6 Molecular Engineering, Peking University, Beijing 100871, P. R. China.

7 ²School of Materials Science and Engineering, Nanyang Technological University,
8 Singapore 639798, Singapore.

9 ³College of Environmental Sciences and Engineering, The Key Laboratory of Water
10 and Sediment Sciences (Ministry of Education), Peking University, Beijing 100871, P.
11 R. China.

12 ⁴Department of Chemistry, Tsinghua University, Beijing 100084, P. R. China.

13 ⁵These authors contributed equally: Xueting Feng and Jiyuan Liu.

14 **Abstract**

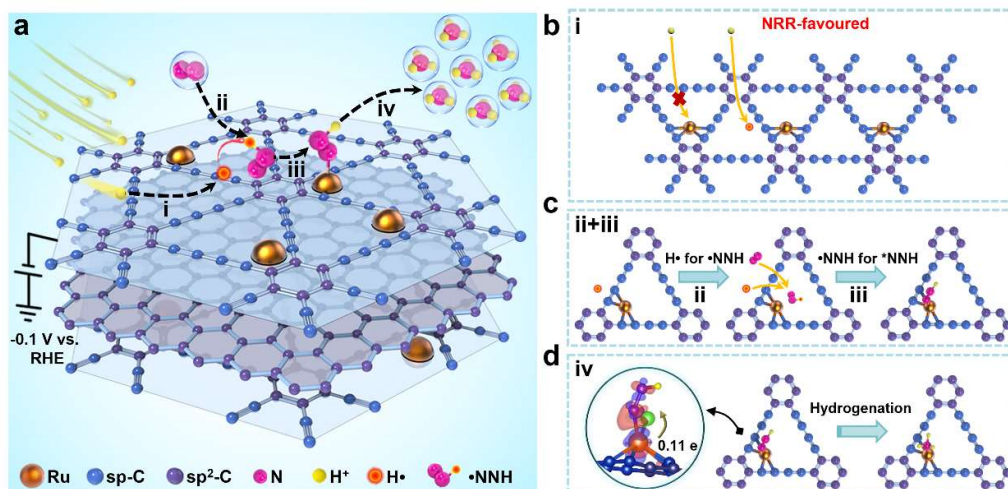
15 Realizing efficient hydrogenation of N_2 molecules in the electrocatalytic nitrogen
16 reduction reaction (NRR) is crucial in achieving high activity at low potential because
17 it theoretically requires a higher equilibrium potential than other steps. Analogous to
18 metal hydride complexes for N_2 reduction, achieving this step by chemical
19 hydrogenation can weaken the potential dependence of the initial hydrogenation
20 process. However, this strategy is rarely reported in electrocatalytic NRR, and the
21 catalytic mechanism remains ambiguous and lacks experimental evidence. Here we
22 show a highly efficient electrocatalyst (ruthenium single atoms anchored on
23 graphdiyne/graphene sandwich structures) with a hydrogen radicals-transferring
24 mechanism, in which graphdiyne (GDY) generates hydrogen radicals ($H\cdot$), which can
25 effectively activate N_2 to generate NNH radicals ($\cdot NNH$). A dual-active site is
26 constructed to suppress competing hydrogen evolution, where hydrogen preferentially
27 adsorbs on GDY and Ru single atoms serve as the adsorption site of $\cdot NNH$ to promote
28 further hydrogenation of NH_3 synthesis. As a result, a high activity and selectivity are
29 obtained simultaneously at -0.1 V versus a reversible hydrogen electrode. Our findings
30 illustrate a novel hydrogen transfer mechanism that can greatly reduce the potential and
31 maintain the high activity and selectivity in NRR, and provide powerful guidelines for
32 design concept of electrocatalysts.

33 **Introduction**

34 Electrocatalytic NRR generally suffers from poor NH₃ selectivity and activity due to
35 the competitive hydrogen evolution and high reaction barrier^{1, 2}. From the
36 thermodynamic perspective, it typically proceeds at a potential similar to that required
37 for the hydrogen evolution reaction (HER), accounting for the extremely low Faradaic
38 efficiency (FE) towards NH₃ synthesis³⁻⁵. Especially at large potential, HER is more
39 likely to occur. From the kinetic view, the formation of *NNH (* represents the catalyst
40 surface sites), which is widely considered as a rate-limiting step, limits the
41 improvement of NRR activity due to its relatively large energy barrier⁶⁻⁹. Accordingly,
42 it is imperative to construct an electrocatalyst that could balance the competition
43 between H and N₂ on the active site and accelerate the reaction kinetics of
44 hydrogenation process, thereby enhancing the NRR activity at low potential. As shown
45 in Fig. 1a, an NRR electrocatalyst of Ru single atoms (Ru SAs) on graphdiyne/graphene
46 sandwich structures (GDY/G) is designed. Ru, as a second-generation NH₃ catalyst, has
47 shown high activity towards NRR due to the appropriate N₂ adsorption energy and
48 required potential much lower than that of other precious metals^{10, 11}. Recently, single-
49 atom catalysts with atomically dispersed metal active centers have attracted extensive
50 research interest due to their maximum atomic efficiency¹². These catalysts have well-
51 defined active sites, providing a unique opportunity to further understand the reaction
52 mechanism on the active sites¹³. Due to the unique atomic structures and electronic
53 properties, single-atom catalysts exhibit extremely excellent catalytic activity and
54 selectivity in many electrocatalytic reactions^{14, 15}. For example, Ru single-atom

55 catalysts enable high FE due to the lower adsorption capacity of H than that on metal
56 particles or clusters^{16, 17}. Graphdiyne (GDY), a carbon allotrope composed of sp² and
57 sp-hybrid carbon atoms, has high intrinsic activity for HER due to uneven surface
58 charge distribution compared with several other carbon materials, such as graphene,
59 carbon nanotubes, fullerenes^{18, 19}. Thus, an electrocatalyst with dual-active sites is
60 constructed, where H adsorption and N₂ hydrogenation process take place at spatially
61 separated sites, respectively. Here, the H⁺ preferentially attacks GDY rather than Ru
62 single atoms, effectively inhibiting the coverage of H at the Ru active sites, thus
63 improving the FE of NRR process (Fig. 1b). Furthermore, we show that the GDY can
64 generate hydrogen radicals (H•), and a new mechanism via H• transfer pathway is
65 proposed that expedites the reaction kinetics of hydrogenation process. In brief, the
66 combined effect of both the dual-active sites and the H•-transferring mechanism leads
67 to high activity and selectivity simultaneously on Ru SAs/GDY/G catalyst at low
68 potential (-0.1 V versus a reversible hydrogen electrode).

69 The whole design concept of NRR on Ru SAs/GDY/G catalyst goes through the
70 following steps (Fig. 1a). The GDY can generate H• (step i). H• can react with N₂ to
71 form NNH radicals (•NNH) and then the •NNH adsorbs on Ru single atoms to form
72 *NNH (step ii and iii in Fig. 1c). Subsequently, *NNH goes through a step-by-step
73 hydrogenation to form *NH₃ and then desorbs to form NH₃ (step iv in Fig. 1d).



74

75 **Fig. 1 Conceptual diagram of N₂ electroreduction to ammonia (NH₃) on Ru**
 76 **SAs/GDY/G.** Ru SAs/GDY/G stands for ruthenium single atoms (Ru SAs) anchored
 77 on graphdiyne/graphene sandwich structures (GDY/G). **a** Proposed reaction scheme for
 78 N₂ electroreduction to NH₃ on Ru SAs/GDY/G. **b** Mass transfer of protons to the Ru
 79 SAs/GDY/G surface in electrolytes. **c** Schematic representation of the •NNH generation
 80 mechanism and *NNH adsorption configurations on Ru single atom. **d** The
 81 hydrogenation of NH₃ synthesis on Ru single atom and the charge density fluctuations
 82 of *NNH adsorption configurations (charge density accumulation and depletion
 83 depicted in orange and blue, respectively).

84 Results and Discussion

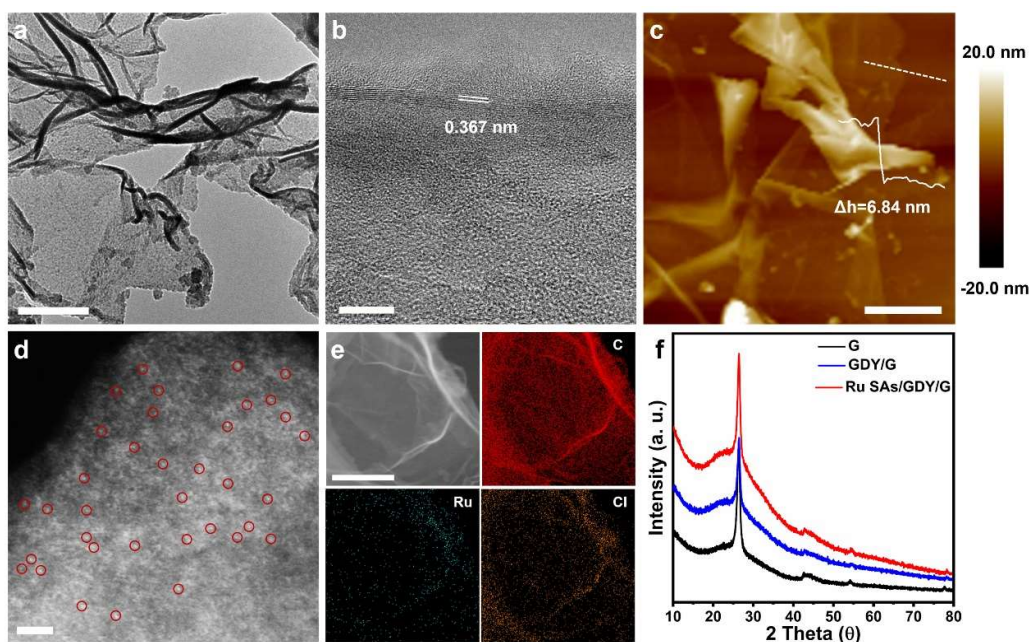
85 Synthesis and characterization of catalysts

86 The Ru SAs/GDY/G catalyst was synthesized through a simple impregnation method
 87 on the graphdiyne/graphene sandwich structures (Supplementary Fig. S1). Briefly, the
 88 GDY/G was fabricated via Eglinton coupling reaction using a fast, simple and efficient
 89 microwave synthesis²⁰. This strategy involves mixing Cu(OAc)₂·H₂O and graphene
 90 with monomer hexaethynylbenzene (HEB) at room temperature, followed by
 91 microwave radiation of the mixture for only 1 min in the household microwave oven.

92 The photograph of as-prepared GDY/G powder is shown in Supplementary Fig. S2a.
93 X-ray photoelectron spectroscopy (XPS) and inductively coupled plasma mass
94 spectrometry (ICP-MS) analysis confirm that only a very small amount of copper
95 remains in the GDY/G, with a content of 0.16 wt% (Supplementary Fig. S2b). The
96 residual copper has no effect on electrocatalytic performance, which will be discussed
97 later in this work. The XPS C 1s spectrum of GDY/G is deconvoluted into four peaks
98 at 284.4, 285.0, 286.4, and 288.5 eV, assigning to C-C (sp^2), C-C (sp), C-O, and C=O,
99 respectively (Supplementary Fig. S3)²¹. From the GDY structural model, the theoretical
100 ratio of sp to sp^2 carbon atoms should be 2. However, the experimentally obtained ratio
101 is less than 2 due to the existence of graphene²⁰. Transmission electron microscopy
102 (TEM) image of GDY/G indicates a lamellar structure, in which the smooth surface of
103 graphene is covered by GDY thin film (Fig. 2a and Supplementary Fig. S4a). The high-
104 resolution TEM (HRTEM) in Supplementary Fig. S5 shows a well-defined interface
105 between GDY and graphene, further elaborating that the GDY film grows in-plane on
106 graphene. Due to the van der Waals interaction and lattice match between GDY and
107 graphene, the GDY thin film uniformly distributed on both sides of the graphene²². In
108 the absence of graphene, the GDY samples obtained by the same strategy are severely
109 stacked (Supplementary Fig. S6a-c), confirming the importance of graphene as
110 template in GDY growth. Additionally, the interlayer space of 0.367 nm and 0.366 nm
111 are observed at the edges of the GDY/G and GDY, respectively, which is classified to
112 the interlayer space of GDY (Fig. 2b and Supplementary Fig. S6d). Atomic force
113 microscopy (AFM) image (Fig. 2c) suggests that the thickness of GDY/G is about 6.84

114 nm, in which the thickness of graphene is 2.74 nm (Supplementary Fig. S4b). Therefore,
115 it can be calculated that the thickness of the GDY film on the graphene side is about
116 2.05 nm. Afterwards, the Ru SAs/GDY/G was obtained by impregnation method, and
117 its morphology was first characterized by TEM in Supplementary Fig. S7. It shows a
118 sandwiched-like structure originating from GDY/G, and no obvious Ru nanoparticles
119 or clusters can be observed on the GDY/G scaffold. From the aberration-corrected high-
120 angle annular dark-field scanning transmission electron microscopy (HAADF-STEM)
121 (Fig. 2d), isolated Ru single atoms anchored on the GDY/G can be clearly assigned as
122 bright dots. The content of Ru is estimated to be 1.8 wt% based on ICP-MS analysis,
123 which is in agreement with the results of energy-dispersive X-ray spectroscopy (EDX)
124 (1.5 wt%, Supplementary Fig. S8). EDX mapping analysis in Fig. 2e reveals the
125 existence of Ru, C, and Cl elements throughout the Ru SAs/GDY/G and the uniform
126 dispersion of Ru element in the GDY/G. The X-ray diffraction (XRD) patterns of Ru
127 SAs/GDY/G in Fig. 2f indicate that there are no peaks related to Ru-based crystals,
128 further demonstrating the single-atomic nature of Ru in Ru SAs/GDY/G. The XRD
129 patterns of Ru SAs/GDY/G and GDY/G are similar. A broad peak over 23° corresponds
130 to the interlayer distance of GDY²³, and two peaks at 26.2 and 54.0 are ascribed to the
131 (002) and (004) planes of graphitic carbon²⁴. For comparison, the Ru nanoparticles on
132 graphene sheet (Ru NPs/G) control sample was prepared and characterized. ICP-MS
133 analysis shows that the Ru content in the Ru NPs/G is 8.4 wt%. The Ru nanoparticles
134 are distributed in the graphene matrix with a highly agglomerated distribution, and a
135 clearly visible crystal structure of Ru nanoparticles is illustrated in Supplementary Fig.

136 S9. The corresponding fast-Fourier transform (FFT) exhibits that the lattice spacing of
137 0.214 nm is attributed to the (002) plane of hexagonal Ru. The specific surface area and
138 pore volume of Ru SAs/GDY/G are $211.20 \text{ m}^2 \text{ g}^{-1}$ and $0.37 \text{ cm}^3 \text{ g}^{-1}$, respectively, which
139 is higher than that of Ru NPs/G ($98.68 \text{ m}^2 \text{ g}^{-1}$ and $0.26 \text{ cm}^3 \text{ g}^{-1}$, Supplementary Fig.
140 S10).

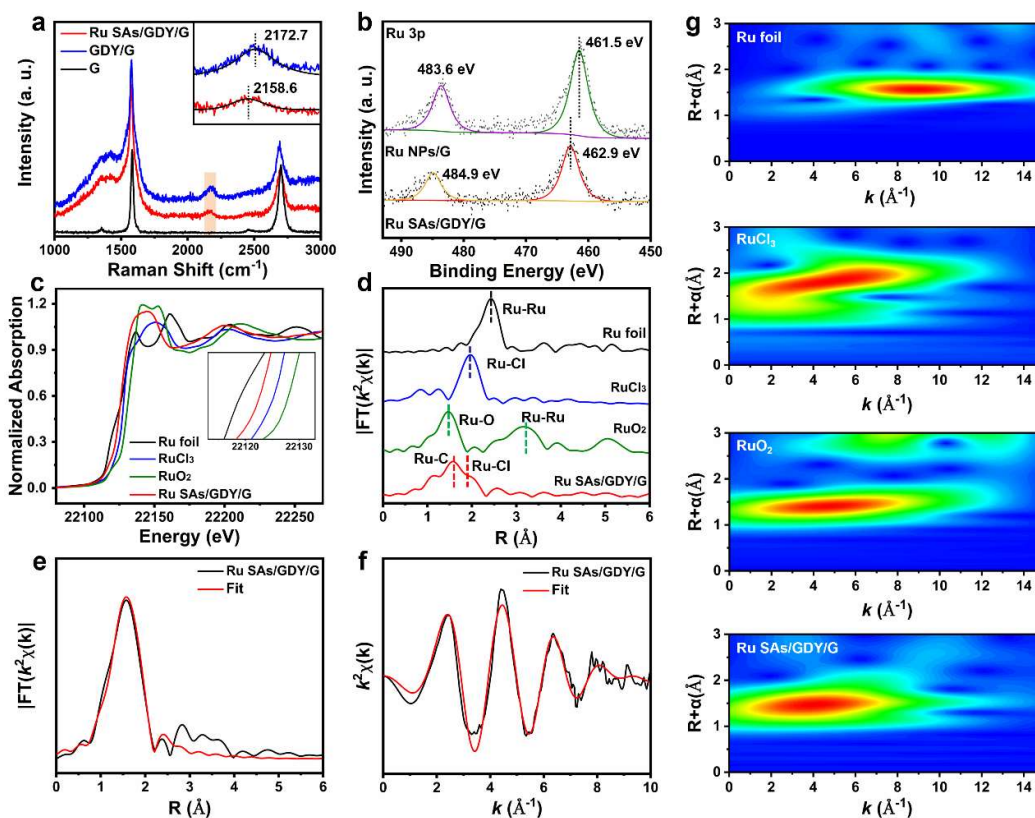


141
142 **Fig. 2 Characterizations of GDY/G and Ru SAs/GDY/G.** GDY/G stands for
143 graphdiyne/graphene sandwich structures. **a** Transmission electron microscopy (TEM)
144 image of GDY/G. Scale bar, 500 nm. **b** High-resolution TEM (HRTEM) image of
145 GDY/G. Scale bar, 10 nm. **c** Atomic force microscopy (AFM) image of GDY/G. Scale
146 bar, 500 nm. **d** Aberration-corrected high-angle annular dark-field scanning
147 transmission electron microscopy (HAADF-STEM) image of Ru SAs/GDY/G. Some
148 of Ru single atoms are indicated by the red circles. Scale bar, 2 nm. **e** HAADF-STEM
149 image and corresponding EDX elemental mapping images of Ru SAs/GDY/G, C (red),
150 Ru (cyan), and Cl (orange). Scale bar, 300 nm. **f** X-ray diffraction (XRD) patterns of
151 Ru SAs/GDY/G, GDY/G and G. G stands for graphene sheet.

152 The structure of catalysts was further investigated by Raman spectroscopy, XPS and X-

153 ray absorption spectroscopy (XAS). Fig. 3a shows Raman spectra of Ru SAs/GDY/G,
154 GDY/G and G. The distinct peaks at approximately 1353.1, 1583.2 and 2701.1 cm^{-1} are
155 assigned as D band, G band and 2D band of graphene, respectively. The Y peak centered
156 at 2158.6 and 2172.7 cm^{-1} in the Ru SAs/GDY/G and GDY/G is attributed to the triple
157 bond vibration of the diacetylenic linkages ($-\text{C}\equiv\text{C}-\text{C}\equiv\text{C}-$) in GDY. The obvious red shift
158 suggests the generation of coordination bonds between Ru and C of the diacetylenic
159 linkages in GDY²⁵. XPS analysis shows the presence of oxidized ruthenium on the
160 surface of Ru SAs/GDY/G. In Fig. 3b, the binding energies of Ru $3p_{3/2}$ and Ru $3p_{1/2}$
161 peaks in the Ru SAs/GDY/G are 462.9 and 484.9 eV, respectively, which correspond to
162 the oxidized ruthenium²⁶. Correspondingly, the two peaks appeared at 461.5 and 483.6
163 eV in Ru NPs/G are attributed to the metallic ruthenium²⁷. The binding energies of Ru
164 SAs/GDY/G are higher than that of Ru NPs/G, and lower than that of Ru^{3+} , indicating
165 that the valence states of Ru in the Ru SAs/GDY/G are between 0 and 3²⁶. X-ray
166 absorption fine structure (XAFS) was performed to further reveal the state of the Ru
167 species in the Ru SAs/GDY/G at the atomic level, with Ru foil, RuCl_3 and RuO_2 as
168 reference. In Fig. 3c, the near-edge absorption energy of Ru SAs/GDY/G is situated
169 between Ru foil and RuCl_3 references, further implying that the oxidation state of Ru
170 sits between Ru^0 and Ru^{3+} , and the results are consistent with XPS analysis. The
171 comparison of the k^2 -weighted EXAFS paths is shown in Supplementary Fig. S11. The
172 Fourier transformed k^2 -weighted extended XAFS (FT-EXAFS, without phase
173 correction) spectrum of Ru SAs/GDY/G exhibits two distinct peaks at around 1.56 Å
174 and 1.86 Å, assigning to the Ru-C and Ru-Cl superimposed contribution, respectively

175 (Fig. 3d)^{28, 29}. No obvious Ru-Ru coordination peak at 2.42 Å and other peaks are
176 observed, demonstrating the atomic dispersion of Ru atoms on GDY/G. Moreover, the
177 Cl 2p XPS spectrum further indicates the existence of Cl in Ru SAs/GDY/G
178 (Supplementary Fig. S12a). The atomic dispersed Ru sites of Ru SAs/GDY/G were
179 further confirmed by the wavelet transform (WT)-EXAFS due to its high resolution in
180 both R and k space³⁰. The Ru K-edge WT-EXAFS oscillations in Fig. 3g show one
181 intensity maximum at $\sim 4.1 \text{ \AA}^{-1}$, which corresponding to the first coordination shell of
182 Ru element (Ru-C and Cl coordination). Compared with the WT plots of Ru foil, RuCl₃
183 and RuO₂ references, no intensity maximum arising from Ru-Ru contribution is
184 observed. The above results directly confirm the dispersion of isolated Ru atom in Ru
185 SAs/GDY/G. The EXAFS fitting results show that the Ru-C bond length and Ru-Cl
186 bond length is 2.05 Å and 2.34 Å, respectively, revealing that the Ru atoms anchored
187 on GDY/G are coordinated by four C atoms and a Cl atom (Fig. 3e and f, Supplementary
188 Table S1). The corresponding structure model of Ru SAs/GDY/G is shown in
189 Supplementary Fig. S12b.



190

191 **Fig. 3. Structural analysis of Ru SAs/GDY/G.** **a** Raman spectra of Ru SAs/GDY/G,
 192 GDY/G and G. **b** The high-resolution Ru 3p XPS spectra of Ru SAs/GDY/G and Ru
 193 NPs/G. Ru NPs/G stands for ruthenium nanoparticles on graphene sheet. **c** X-ray
 194 absorption near-edge structure (XANES) spectra and **d** Fourier transformed (FT) k^2 -
 195 weighted $\chi(k)$ -function of the EXAFS spectra at the Ru K-edge of Ru SAs/GDY/G,
 196 referenced Ru foil, RuCl₃ and RuO₂. **e** EXAFS fitting curves of Ru SAs/GDY/G at R-
 197 space. **f** EXAFS fitting curves of Ru SAs/GDY/G at k -space. **g** Wavelet transform (WT)
 198 for the k^2 -weighted EXAFS signals of the Ru K-edge.

199 **Electrocatalytic N₂ reduction performance**

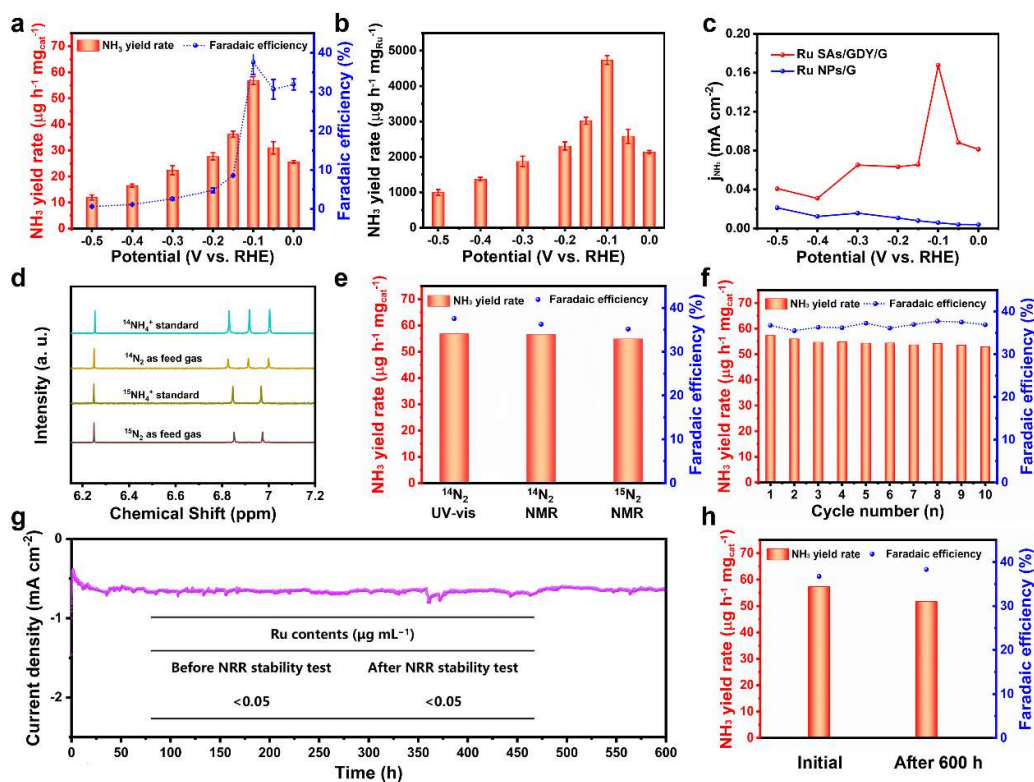
200 The electrochemical nitrogen reduction reaction (NRR) was conducted in a customized
 201 H-cell separated by a Nafion 117 membrane at room temperature (Supplementary Fig.
 202 S13). Based on the rigorous experimental protocol, a series of tests were carried out to
 203 obtain reliable evidence of NRR activity³¹. The produced ammonia was analyzed and

204 quantified by spectrophotometric and NMR methods. As shown in Supplementary Fig.
205 S14-19, no NH₃ and NO_x contaminants are observed in the fully purified gas (¹⁴N₂ and
206 ¹⁵N₂). Moreover, no NH₃ contaminant was detected in the electrolyte (1) bubbled by
207 purified N₂ or Ar without applying potential for 1 h, (2) saturated by purified N₂ or Ar
208 under open circuit potential (OCP) for 1 h, (3) saturated by purified Ar at different
209 applied potentials for 1 h (Supplementary Fig. S20 and 21). To assess the NRR
210 performance of catalysts, linear sweep voltammetry (LSV) was carried out in Ar versus
211 N₂-saturated acidic sodium sulfate electrolytes (pH 2.2, 0.5 M Na₂SO₄), and all
212 potentials were converted to reversible hydrogen electrode (RHE) by experimental
213 calibration (Supplementary Fig. S22). Remarkably, the clear differences of current
214 density for Ru SAs/GDY/G can be observed in Ar and N₂-saturated electrolytes
215 (Supplementary Fig. S23a), indicating the electrochemical responses for NRR³², which
216 is larger than that of Ru NPs/G (Supplementary Fig. S23b). The NH₃ production and
217 possible byproduct N₂H₄ in the electrolyte were quantified, and no byproduct N₂H₄ was
218 detected during NRR test (Supplementary Fig. S24 and S25). Then,
219 chronoamperometry measurements were conducted to further systematically study the
220 NRR activity of Ru SAs/GDY/G with continuous N₂ bubbling (Supplementary Fig.
221 S26a), and the corresponding UV-vis absorption spectra are shown in Supplementary
222 Fig. S26b. The average NH₃ yield rate and FE of Ru SAs/GDY/G are exhibited in Fig.
223 4a. Strikingly, the highest NH₃ yield rate of 56.8 μg h⁻¹ mg_{cat.}⁻¹ (4.7 mg h⁻¹ mg_{Ru}⁻¹) with
224 a FE of 37.6% was achieved at an applied potential of -0.1 V vs. RHE, nearly 6.1 and
225 5.0 times than that of Ru NPs/G, respectively (Fig. 4b and Supplementary Fig. S27).

226 Such NH_3 yield rate and selectivity achieved simultaneously at low potential
227 outperforms most of previously reported work (Supplementary Table S2). Additionally,
228 the NRR activity of Ru SAs/GDY/G was also evaluated in 0.5 M Na_2SO_4 and 0.1 M
229 KOH. As shown in Supplementary Fig. S28, the Ru SAs/GDY/G catalyst exhibits a
230 remarkable NH_3 yield rate of $57.6 \mu\text{g h}^{-1} \text{mg}_{\text{cat.}}^{-1}$ at -0.15 V and FE of 31.5 % at -0.1 V
231 in 0.5 M Na_2SO_4 , and shows a maximum NH_3 yield rate of $60.1 \mu\text{g h}^{-1} \text{mg}_{\text{cat.}}^{-1}$ at -0.2
232 V and FE of 32.4 % at 0 V in 0.1 M KOH. From the above results, it is found that the
233 Ru SAs/GDY/G catalyst can effectively catalyze the NRR in acidic sodium sulfate
234 electrolyte, 0.5 M Na_2SO_4 and 0.1 M KOH, and the required potential is the lowest in
235 acidic sodium sulfate electrolyte. As shown in Fig. 4c, the highest partial current density
236 of 0.17 mA cm^{-2} over the Ru SAs/GDY/G catalyst is almost eight times than that of the
237 Ru NPs/G (0.02 mA cm^{-2}). Interestingly, sole GDY/G shows no detectable NH_3
238 production at different applied potentials (Supplementary Fig. S29a), whereas
239 anchoring Ru single atoms on GDY/G enable the NRR significantly, indicating that
240 GDY/G is inert for NRR process and the single-atom dispersed Ru is regarded as main
241 active site for NRR. Additionally, we also evaluated the NRR performance of GDY/G
242 at different pH values, showing almost no NH_3 formation (Supplementary Fig. S29b
243 and c). Thus, we conclude that the residual copper in GDY/G has no effect on
244 electrocatalytic NH_3 production. For further confirmation of N source and accurate
245 quantification of the NH_3 product from Ru SAs/GDY/G during NRR, isotope labelling
246 experiments were performed. The ^1H nuclear magnetic resonance (NMR) spectra show
247 that a doublet signal corresponding to $^{15}\text{NH}_4^+$ and triple signal representing $^{14}\text{NH}_4^+$ are

248 observed when using $^{15}\text{N}_2$ and $^{14}\text{N}_2$ as gas supply, respectively, revealing that the
249 feeding gas is the only N source (Fig. 4d). The NH_3 yield rate and FE determined by
250 NMR are $56.6 \mu\text{g h}^{-1} \text{mg}_{\text{cat.}}^{-1}$ and 36.3 % using $^{14}\text{N}_2$ as gas, and $54.9 \mu\text{g h}^{-1} \text{mg}_{\text{cat.}}^{-1}$ and
251 35.2% using $^{15}\text{N}_2$ as gas at -0.1 V for Ru SAs/GDY/G, revealing the reliability of
252 quantitative tests (Fig. 4e and Supplementary Fig. S30-32). Moreover, amount of
253 accumulated NH_3 quantified by spectrophotometric and NMR methods shows a good
254 linear increase with the prolongation of reaction time when $^{14}\text{N}_2$ is used (Supplementary
255 Fig. S33), suggesting the stability of NH_3 production rate. The enhanced NRR activity
256 of Ru SAs/GDY/G was confirmed by electrochemically active surface area (ECSA)
257 and electrochemical impedance spectroscopy (EIS) measurement. The ECSA assessed
258 by the double layer capacitance (C_{dl})³³ are shown in Supplementary Fig. S34a-c. The
259 determined C_{dl} of Ru SAs/GDY/G and Ru NPs/G are 6.32 and 2.26 mF cm^{-2} ,
260 respectively, revealing more exposed active sites for Ru SAs/GDY/G. The charge
261 transfer resistance (R_{ct}) of the Ru SAs/GDY/G is much smaller than that of Ru NPs/G,
262 which could favor charge transfer and thus enhance NRR kinetics (Supplementary Fig.
263 S34d). The GDY/G possesses a faster charge transfer capacity than GDY, implying that
264 the graphene can not only serve as a template for GDY growth, but also improve the
265 conductivity of the catalyst. Furthermore, both NH_3 yield rate and FE of the Ru
266 SAs/GDY/G exhibit no significant variation through ten consecutive tests (Fig. 4f and
267 Supplementary Fig. S35). During the long-term electrocatalysis for 600 h at -0.1 V, the
268 current density of the Ru SAs/GDY/G hardly attenuates (Fig. 4g). It just shows a trivial
269 loss in NH_3 yield rate and slight increase in FE after 600 h stability test, confirming the

270 superior electrochemical durability (Fig. 4h). Careful examination of TEM, aberration-
 271 corrected HAADF-STEM (Supplementary Fig. S36), EDX (Supplementary Fig. S37
 272 and 38), Raman and XPS spectra (Supplementary Fig. S39) and XAS spectra
 273 (Supplementary Fig. S40) display that the morphology and structure of the Ru
 274 SAs/GDY/G remain unchanged after cycling test, confirming its robustness towards
 275 NH₃ synthesis. Importantly, no Ru species in the electrolyte solution are detected after
 276 600 h stability test on the Ru SAs/GDY/G under -0.1 V, which reveal the excellent
 277 stability of Ru single atoms. The above results show that the Ru SAs/GDY/G
 278 simultaneously obtains high FE and NH₃ yield rate, as well as superior stability.



279
 280 **Fig. 4. Electroreduction of N₂ to NH₃ under ambient conditions.** **a** NH₃ yield rate
 281 and Faradaic efficiency (FE) of Ru SAs/GDY/G at selected potentials. **b** NH₃ yield rate
 282 normalized by the mass of Ru for Ru SAs/GDY/G at different potentials. **c** Partial

283 current densities (j_{NH_3}) of NRR at different applied potentials of Ru SAs/GDY/G and
284 Ru NPs/G. **d** ^1H NMR spectra of the NRR products using different feed gases. **e**
285 Comparison of the calculated NH_3 yield rate and FE at -0.1 V by NMR and UV-vis
286 methods. **f** Cycling test and **g** stability test of Ru SAs/GDY/G at -0.1 V. Inset: the Ru
287 contents in electrolytes before and after 600 h stability. **h** NH_3 yield rate and FE of
288 initial and after 600 h stability test.

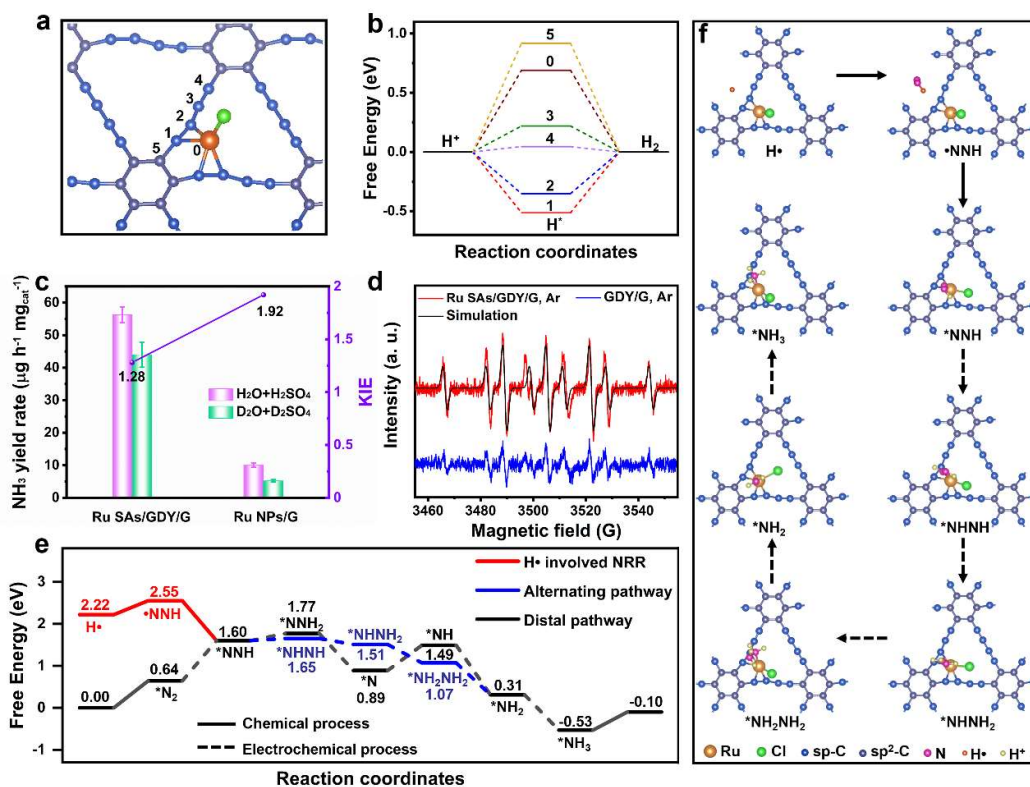
289 **The mechanism of electrocatalytic NRR**

290 We performed density functional theory (DFT) calculations to further explain the
291 mechanism of NRR on the Ru SAs/GDY/G. The NRR selectivity was also investigated.
292 The predominance of H adsorption over N_2 adsorption is believed to be the main reason
293 for the potential-dependent decrease in NRR activity^{34, 35}. Notably, N_2 preferentially
294 adsorbs on Ru active site compared to the other active sites (Supplementary Fig. S41
295 and 42). The H adsorption is significantly suppressed on Ru active site with high free-
296 energy change of 0.69 eV, and thus effectively suppressing the competitive HER (Fig.
297 5a-b and Supplementary Fig. S43). To further unravel the mechanism of NRR on Ru
298 SAs/GDY/G, kinetic isotope effect (KIE) experiments were carried out to describe the
299 rate-determining step^{36, 37}. Fig. 5c shows that the NH_3 yield rate of both Ru SAs/GDY/G
300 and Ru NPs/G decrease when the $\text{H}_2\text{O}/\text{H}_2\text{SO}_4$ solvent is replaced by $\text{D}_2\text{O}/\text{D}_2\text{SO}_4$
301 solvent. The KIE values of both Ru SAs/GDY/G and Ru NPs/G are greater than 1,
302 indicating that the hydrogenation step is a rate-determining step³⁸. Furthermore, the
303 lower KIE value (1.28) of Ru SAs/GDY/G shows excellent proton transfer kinetics
304 compared to Ru NPs/G (1.92), which accelerates the hydrogenation step in NRR. Here,
305 for the first time, we discovered that GDY could generate $\text{H}\cdot$ through *in situ* electron

306 paramagnetic resonance (EPR) technology. 5,5-dimethyl-1-pyrrolidine-N-oxide
307 (DMPO) as a radical trapping reagent was tested to rule out the possible interference,
308 and no EPR peaks are observed before electrochemical test (Supplementary Fig. S44a).
309 Nine characteristic peaks with an intensity ratio of 1:1:2:1:2:1:2:1:1 are clearly
310 observed for both GDY/G and Ru SAs/GDY/G under Ar atmosphere at -0.1 V (Fig. 5d),
311 which are consistent with the simulation results and are assigned to DMPO-•H ($A_N =$
312 22.8 G, $A_H = 16.5$ G)^{39, 40}. In comparison, no EPR signal obtained for the graphene
313 (Supplementary Fig. S44b) reveals that the formation of H• in GDY/G is attributed to
314 GDY. In order to reveal the source of H•, isotope experiments of GDY/G were carried
315 out with D₂O/D₂SO₄ electrolyte instead of H₂O/H₂SO₄ electrolyte. The captured signal
316 was assigned to DMPO-•D, with the typical characteristic parameter of $A_N = 16.7$ G,
317 $A_H = 22.7$ G, $A_D = 3.5$ G, and no EPR peaks corresponding to DMPO-•H are observed,
318 indicating that the hydrogen source of the hydrogen radicals comes from the electrolyte
319 (Supplementary Fig. S45). The Ru SAs/GDY/G possesses stronger DMPO-•H signal
320 than that of the GDY/G, whereas Ru NPs/G does not generate H• (Supplementary Fig.
321 S46a). When the electrocatalysis is operated under N₂ atmosphere, the DMPO-•H
322 signal becomes undetectable and the new signal corresponding to •NNH_x ($A_N = 13.9$ G,
323 $A_H = 8.5$ G, and $A_N = 1.5$ G) is presented for Ru SAs/GDY/G (Supplementary Fig.
324 S46b), which suggests that the H• generated by GDY is rapidly consumed to participate
325 NRR process. Taken together, the above results indicate that the hydrogenation process
326 of NRR for Ru SAs/GDY/G involves a new mechanism via H• transfer pathway. DFT
327 computational studies further confirm the proposed mechanism. As previously reported

328 in the literature, the enzymatic, distal and alternating pathways are possible mechanisms
329 of NRR⁴¹. Due to that the N₂ molecule cannot be stabilized as the side-on configuration
330 on the Ru single atom of the Ru SAs/GDY/G, which is suggested by the DFT
331 calculation, the enzymatic pathway is not considered in this work. It shows that the
332 alternating pathway is more favorable than the distal pathway with the optimal end-on
333 adsorption configuration of N₂ (Supplementary Fig. S42). As shown in Fig. 5e, the Ru
334 SAs/GDY/G exhibits a particularly high free-energy change of 0.64 eV, revealing the
335 difficult adsorption of N₂ on its surface. The corresponding first-hydrogenation energy
336 is even higher ($\Delta G_r(*N_2 \rightarrow *NNH) = 0.96$ eV), indicating the whole activating process
337 of N₂ is thermodynamically forbidden if only the Ru single atom is involved, which is
338 nevertheless conflict with our experiments. With the assistance of H•, our calculation
339 suggests the first-hydrogenation of the N₂ molecule becomes much easier
340 ($\Delta G_r(H\bullet \rightarrow \bullet NNH) = 0.33$ eV). It is obvious that the H• can effectively activate N₂ to
341 generate •NNH, which is consistent with the captured •NNH_x in the experimental
342 results (Supplementary Fig. S46b). Thus, we speculate that the NRR process undergoes
343 a H• transfer pathway with significantly decreased free-energy gap (Fig. 5f). The first
344 step is the activation of the N₂ molecule by H•, giving rise to the •NNH, followed by
345 the exothermic •NNH adsorption (*NNH) on Ru. Subsequently, the stepwise
346 hydrogenation of *NNH occurs through the alternating pathway, which is
347 thermodynamically more favorable than that through the distal pathway (Fig. 5f and
348 Supplementary Fig. S47). Moreover, the hydrogenation of *NNH to *NHNH is the
349 potential-determining step (PDS) of 0.05 eV, which determines the onset potential of

350 NRR⁴². Thus, it can be seen that the corresponding calculated onset potential is -0.05
 351 V, further confirming the superior catalytic activity of NRR towards Ru SAs/GDY/G at
 352 -0.1 V. Consequently, the dual-active sites and hydrogen radicals-transferring
 353 mechanism result in the improved FE and NH₃ yield rate on Ru SAs/GDY/G.



354
 355 **Fig. 5. Insights into the mechanism of NRR on Ru SAs/GDY/G.** **a** The structure of
 356 Ru SAs/GDY/G. **b** Free energy diagram of the intermediates generated during HER
 357 over the Ru SAs/GDY/G at different active sites annotated in Fig. 5a. **c** KIE of H/D and
 358 NH₃ yield rate over Ru SAs/GDY/G and Ru NPs/G at -0.1 V. **d** EPR spectra of the
 359 solutions obtained after 10 min NRR tests by Ru SAs/GDY/G and GDY/G under Ar. **e**
 360 Free energy diagrams of NRR on Ru SAs/GDY/G. **f** The structure of the intermediates
 361 for the H• involved NRR process.

362 Conclusions

363 Our finding demonstrates that Ru SAs/GDY/G is an efficient electrocatalyst for NRR,

364 showing an exceptionally high NH_3 yield rate of $56.8 \mu\text{g h}^{-1} \text{mg}_{\text{cat.}}^{-1}$ ($4.7 \text{mg h}^{-1} \text{mg}_{\text{Ru}}^{-1}$)
365 and FE of 37.6% at -0.1 V. The experiments and DFT calculations suggest that the Ru
366 single atoms function as active sites for hydrogenation process of NRR. The GDY not
367 only inhibits H covering on Ru single atoms, but also produces $\text{H}\cdot$ to accelerate the
368 kinetics of hydrogenation process. To our knowledge, the $\text{H}\cdot$ -transferring mechanism
369 is a wholly new observation in NRR. Our designed catalysts are conceptually similar,
370 opening new possibilities for the design of highly selective and active electrocatalysts
371 for electrocatalytic hydrogenation reactions.

372 **ASSOCIATED CONTENT**

373 **Supporting Information**

374 Experimental section, construction of models and computation details, structural
375 characterization, photograph of setup for NRR measurement, additional
376 electrochemical results and performance comparison.

377 **AUTHOR INFORMATION**

378 Corresponding Author

379 **Jin Zhang** - Center for Nanochemistry, Beijing Science and Engineering Center for
380 Nanocarbons, Beijing National Laboratory for Molecular Sciences, College of
381 Chemistry and Molecular Engineering, Peking University, Beijing 100871, P. R. China. ;
382 Email: jinzhang@pku.edu.cn

383 **Lianming Tong** - Center for Nanochemistry, Beijing Science and Engineering Center
384 for Nanocarbons, Beijing National Laboratory for Molecular Sciences, College of
385 Chemistry and Molecular Engineering, Peking University, Beijing 100871, P. R. China. ;
386 Email: tonglm@pku.edu.cn

387 **Shuzhou Li** - School of Materials Science and Engineering, Nanyang Technological
388 University, Singapore 639798, Singapore; Email: lisz@ntu.edu.sg

389 **Notes**

390 The authors declare no competing interests.

391 **Acknowledgements**

392 The authors thank Prof. D. Ma for helpful discussion and Ms L. Wang at Peking
393 University for her help with NMR studies. This work was financially supported by the

394 Ministry of Science and Technology of China (2018YFA0703502 and
395 2016YFA0200104), the National Natural Science Foundation of China (Grant Nos.
396 51720105003, 21790052, 52021006, 21974004, T2188101), the Strategic Priority
397 Research Program of CAS (XDB36030100), the Beijing National Laboratory for
398 Molecular Sciences (BNLMS-CXTD-202001), the China Postdoctoral Science
399 Foundation (Grant Nos. 8206300625 and 8206400103), and the Academic Research
400 Fund Tier 1 (No. RG10/21). We thank the computing resources from National
401 Supercomputing Centre Singapore.

402 **References**

- 403 (1) Pang, Y.; Su, C.; Jia, G.; Xu, L.; Shao, Z. Emerging two-dimensional nanomaterials for
404 electrochemical nitrogen reduction. *Chem. Soc. Rev.* **2021**, *50*, 12744-12787.
- 405 (2) Guo, W.; Zhang, K.; Liang, Z.; Zou, R.; Xu, Q. Electrochemical nitrogen fixation and utilization:
406 theories, advanced catalyst materials and system design. *Chem. Soc. Rev.* **2019**, *48*, 5658-5716.
- 407 (3) Garrido-Barros, P.; Derosa, J.; Chalkley, M. J.; Peters, J. C. Tandem electrocatalytic N₂ fixation via
408 proton-coupled electron transfer. *Nature* **2022**, *609*, 71-76.
- 409 (4) Hiang Kwee Lee; Charlynn Sher Lin Koh; Yih Hong Lee; Chong Liu; In Yee Phang; Xuemei Han;
410 Chia-Kuang Tsung; Ling, X. Y. Favoring the unfavored: Selective electrochemical nitrogen fixation using
411 a reticular chemistry approach. *Sci. Adv.* **2018**, *4*, 3208-3215.
- 412 (5) Wang, M.; Liu, S.; Qian, T.; Liu, J.; Zhou, J.; Ji, H.; Xiong, J.; Zhong, J.; Yan, C. Over 56.55%
413 Faradaic efficiency of ambient ammonia synthesis enabled by positively shifting the reaction potential.
414 *Nat Commun* **2019**, *10*, 341.
- 415 (6) Zhu, D.; Zhang, L.; Ruther, R. E.; Hamers, R. J. Photo-illuminated diamond as a solid-state source
416 of solvated electrons in water for nitrogen reduction. *Nat. Mater.* **2013**, *12*, 836-841.
- 417 (7) Fang, Y.; Xue, Y.; Hui, L.; Yu, H.; Zhang, C.; Huang, B.; Li, Y. Graphdiyne-Induced Iron Vacancy for
418 Efficient Nitrogen Conversion. *Adv. Sci.* **2022**, *9*, e2102721.
- 419 (8) Fan, G.; Xu, W.; Li, J.; Chen, J. L.; Yu, M.; Ni, Y.; Zhu, S.; Su, X. C.; Cheng, F. Nanoporous NiSb to
420 Enhance Nitrogen Electroreduction via Tailoring Competitive Adsorption Sites. *Adv. Mater.* **2021**, *33*,
421 e2101126.
- 422 (9) Wang, J.; Yu, L.; Hu, L.; Chen, G.; Xin, H.; Feng, X. Ambient ammonia synthesis via palladium-
423 catalyzed electrohydrogenation of dinitrogen at low overpotential. *Nat. Commun.* **2018**, *9*, 1795.
- 424 (10) Schlogl, R. Catalytic synthesis of ammonia-a "never-ending story"? *Angew. Chem., Int. Ed.* **2003**,
425 *42*, 2004-2008.
- 426 (11) Yao, Y.; Wang, H.; Yuan, X.-z.; Li, H.; Shao, M. Electrochemical Nitrogen Reduction Reaction on
427 Ruthenium. *ACS Energy Lett.* **2019**, *4*, 1336-1341.
- 428 (12) Liang, X.; Fu, N.; Yao, S.; Li, Z.; Li, Y. The Progress and Outlook of Metal Single-Atom-Site
429 Catalysis. *J. Am. Chem. Soc.* **2022**, *144*, 18155-18174.
- 430 (13) Liu, D.; He, Q.; Ding, S.; Song, L. Structural Regulation and Support Coupling Effect of Single-
431 Atom Catalysts for Heterogeneous Catalysis. *Adv. Energy Mater.* **2020**, *10*, 2001482.
- 432 (14) Fang, S.; Zhu, X.; Liu, X.; Gu, J.; Liu, W.; Wang, D.; Zhang, W.; Lin, Y.; Lu, J.; Wei, S.; Li, Y.; Yao,
433 T. Uncovering near-free platinum single-atom dynamics during electrochemical hydrogen evolution
434 reaction. *Nat. Commun.* **2020**, *11*, 1029.
- 435 (15) Zhang, Z.; Zhu, J.; Chen, S.; Sun, W.; Wang, D. Liquid Fluxional Ga Single Atom Catalysts for
436 Efficient Electrochemical CO₂ Reduction. *Angew. Chem., Int. Ed.* **2022**, *62*, e202215136.
- 437 (16) Geng, Z.; Liu, Y.; Kong, X.; Li, P.; Li, K.; Liu, Z.; Du, J.; Shu, M.; Si, R.; Zeng, J. Achieving a
438 Record-High Yield Rate of 120.9 μg_{NH₃} mg_{cat.}⁻¹ h⁻¹ for N₂ Electrochemical Reduction over Ru Single-
439 Atom Catalysts. *Adv Mater* **2018**, *30*, e1803498.
- 440 (17) Tao, H.; Choi, C.; Ding, L.-X.; Jiang, Z.; Han, Z.; Jia, M.; Fan, Q.; Gao, Y.; Wang, H.; Robertson,
441 A. W.; Hong, S.; Jung, Y.; Liu, S.; Sun, Z. Nitrogen Fixation by Ru Single-Atom Electrocatalytic
442 Reduction. *Chem.* **2019**, *5*, 204-214.
- 443 (18) Gao, Y.; Xue, Y.; Qi, L.; Xing, C.; Zheng, X.; He, F.; Li, Y. Rhodium nanocrystals on porous
444 graphdiyne for electrocatalytic hydrogen evolution from saline water. *Nat. Commun.* **2022**, *13*, 5227.

445 (19) Xue, Y.; Huang, B.; Yi, Y.; Guo, Y.; Zuo, Z.; Li, Y.; Jia, Z.; Liu, H.; Li, Y. Anchoring zero valence
446 single atoms of nickel and iron on graphdiyne for hydrogen evolution. *Nat. Commun.* **2018**, *9*, 1460.

447 (20) Gao, X.; Zhu, Y.; Yi, D.; Zhou, J.; Zhang, S.; Yin, C.; Ding, F.; Zhang, S.; Yi, X.; Wang, J.; Tong,
448 L.; Han, Y.; Liu, Z.; Zhang, J. Ultrathin graphdiyne film on graphene through solution-phase van der
449 Waals epitaxy. *Sci. Adv.* **2018**, *4*, 6378-6384.

450 (21) Pan, C.; Wang, C.; Zhao, X.; Xu, P.; Mao, F.; Yang, J.; Zhu, Y.; Yu, R.; Xiao, S.; Fang, Y.; Deng, H.;
451 Luo, Z.; Wu, J.; Li, J.; Liu, S.; Xiao, S.; Zhang, L.; Guo, Y. Neighboring sp-Hybridized Carbon
452 Participated Molecular Oxygen Activation on the Interface of Sub-nanocluster CuO/Graphdiyne. *J. Am.*
453 *Chem. Soc.* **2022**, *144*, 4942-4951.

454 (22) Jiaqiang Li; Lixiang Zhong; Lianming Tong; Yue Yu; Qing Liu; Shuchen Zhang; Chen Yin; Liang
455 Qiao; Shuzhou Li; Rui Si; Zhang, J. Atomic Pd on Graphdiyne/Graphene Heterostructure as Efficient
456 Catalyst for Aromatic Nitroreduction. *Adv. Funct. Mater.* **2019**, *29*, 1905423-1905431.

457 (23) Shang, H.; Zuo, Z.; Yu, L.; Wang, F.; He, F.; Li, Y. Low-Temperature Growth of All-Carbon
458 Graphdiyne on a Silicon Anode for High-Performance Lithium-Ion Batteries. *Adv. Mater.* **2018**, *30*,
459 1801459.

460 (24) Xiao-Chen Dong; Xu, H.; Wang, X.-W.; Huang, Y.-X.; Chan-Park, M. B.; Zhang, H.; Wang, L.-H.;
461 Huang, W.; Chen, P. 3D Graphene-Cobalt Oxide Electrode for High-Performance Supercapacitor and
462 Enzymeless Glucose Detection. *ACS Nano* **2012**, *6*, 3206-3213.

463 (25) Ren, H.; Shao, H.; Zhang, L.; Guo, D.; Jin, Q.; Yu, R.; Wang, L.; Li, Y.; Wang, Y.; Zhao, H.; Wang,
464 D. A New Graphdiyne Nanosheet/Pt Nanoparticle-Based Counter Electrode Material with Enhanced
465 Catalytic Activity for Dye-Sensitized Solar Cells. *Adv. Energy Mater.* **2015**, *5*, 1500296.

466 (26) Hu, Y.; Luo, G.; Wang, L.; Liu, X.; Qu, Y.; Zhou, Y.; Zhou, F.; Li, Z.; Li, Y.; Yao, T.; Xiong, C.;
467 Yang, B.; Yu, Z.; Wu, Y. Single Ru Atoms Stabilized by Hybrid Amorphous/Crystalline FeCoNi Layered
468 Double Hydroxide for Ultraefficient Oxygen Evolution. *Adv. Energy Mater.* **2020**, *11*, 2002816.

469 (27) Yu, B.; Li, H.; White, J.; Donne, S.; Yi, J.; Xi, S.; Fu, Y.; Henkelman, G.; Yu, H.; Chen, Z.; Ma, T.
470 Tuning the Catalytic Preference of Ruthenium Catalysts for Nitrogen Reduction by Atomic Dispersion.
471 *Adv. Funct. Mater.* **2019**, *30*, 1905665.

472 (28) Yu, H.; Hui, L.; Xue, Y.; Liu, Y.; Fang, Y.; Xing, C.; Zhang, C.; Zhang, D.; Chen, X.; Du, Y.; Wang,
473 Z.; Gao, Y.; Huang, B.; Li, Y. 2D graphdiyne loading ruthenium atoms for high efficiency water splitting.
474 *Nano Energy* **2020**, *72*, 104667.

475 (29) Yang, J.; Chen, B.; Liu, X.; Liu, W.; Li, Z.; Dong, J.; Chen, W.; Yan, W.; Yao, T.; Duan, X.; Wu, Y.;
476 Li, Y. Efficient and Robust Hydrogen Evolution: Phosphorus Nitride Imide Nanotubes as Supports for
477 Anchoring Single Ruthenium Sites. *Angew. Chem., Int. Ed.* **2018**, *57*, 9495-9500.

478 (30) Fei, H.; Dong, J.; Arellano-Jimenez, M. J.; Ye, G.; Dong Kim, N.; Samuel, E. L.; Peng, Z.; Zhu, Z.;
479 Qin, F.; Bao, J.; Yacaman, M. J.; Ajayan, P. M.; Chen, D.; Tour, J. M. Atomic cobalt on nitrogen-doped
480 graphene for hydrogen generation. *Nat. Commun.* **2015**, *6*, 8668.

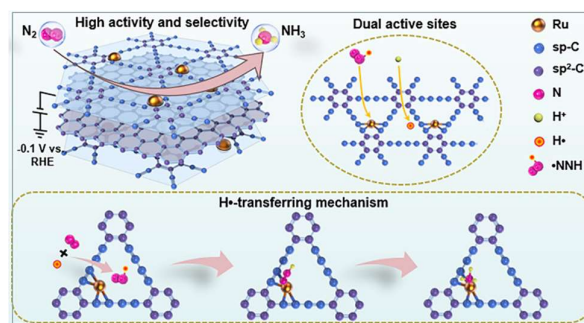
481 (31) Suryanto, B. H. R.; Du, H.-L.; Wang, D.; Chen, J.; Simonov, A. N.; MacFarlane, D. R. Challenges
482 and prospects in the catalysis of electroreduction of nitrogen to ammonia. *Nat. Catal.* **2019**, *2*, 290-296.

483 (32) Li, X.; Shen, P.; Luo, Y.; Li, Y.; Guo, Y.; Zhang, H.; Chu, K. PdFe Single-Atom Alloy Metallene for
484 N₂ Electroreduction. *Angew. Chem., Int. Ed.* **2022**, *61*, e202205923.

485 (33) Dai, J.; Zhu, Y.; Tahini, H. A.; Lin, Q.; Chen, Y.; Guan, D.; Zhou, C.; Hu, Z.; Lin, H. J.; Chan, T. S.;
486 Chen, C. T.; Smith, S. C.; Wang, H.; Zhou, W.; Shao, Z. Single-phase perovskite oxide with super-
487 exchange induced atomic-scale synergistic active centers enables ultrafast hydrogen evolution. *Nat.*
488 *Commun.* **2020**, *11*, 5657.

- 489 (34) Singh, A. R.; Rohr, B. A.; Schwalbe, J. A.; Cargnello, M.; Chan, K.; Jaramillo, T. F.; Chorkendorff,
490 I.; Nørskov, J. K. Electrochemical Ammonia Synthesis-The Selectivity Challenge. *ACS Catal.* **2016**, *7*,
491 706-709.
- 492 (35) Choi, C.; Gu, G. H.; Noh, J.; Park, H. S.; Jung, Y. Understanding potential-dependent competition
493 between electrocatalytic dinitrogen and proton reduction reactions. *Nat. Commun.* **2021**, *12*, 4353.
- 494 (36) Kong, Y.; Li, Y.; Sang, X.; Yang, B.; Li, Z.; Zheng, S.; Zhang, Q.; Yao, S.; Yang, X.; Lei, L.; Zhou,
495 S.; Wu, G.; Hou, Y. Atomically Dispersed Zinc(I) Active Sites to Accelerate Nitrogen Reduction Kinetics
496 for Ammonia Electrosynthesis. *Adv. Mater.* **2022**, *34*, e2103548.
- 497 (37) Liu, H.; Lang, X.; Zhu, C.; Timoshenko, J.; Ruscher, M.; Bai, L.; Guijarro, N.; Yin, H.; Peng, Y.; Li,
498 J.; Liu, Z.; Wang, W.; Cuenya, B. R.; Luo, J. Efficient Electrochemical Nitrate Reduction to Ammonia
499 with Copper-Supported Rhodium Cluster and Single-Atom Catalysts. *Angew. Chem., Int. Ed.* **2022**, *61*,
500 e202202556.
- 501 (38) Fu, H. Q.; Zhou, M.; Liu, P. F.; Liu, P.; Yin, H.; Sun, K. Z.; Yang, H. G.; Al-Mamun, M.; Hu, P.;
502 Wang, H. F.; Zhao, H. Hydrogen Spillover-Bridged Volmer/Tafel Processes Enabling Ampere-Level
503 Current Density Alkaline Hydrogen Evolution Reaction under Low Overpotential. *J. Am. Chem. Soc.*
504 **2022**, *144*, 6028-6039.
- 505 (39) Li, J.; Zhan, G.; Yang, J.; Quan, F.; Mao, C.; Liu, Y.; Wang, B.; Lei, F.; Li, L.; Chan, A. W. M.; Xu,
506 L.; Shi, Y.; Du, Y.; Hao, W.; Wong, P. K.; Wang, J.; Dou, S. X.; Zhang, L.; Yu, J. C. Efficient Ammonia
507 Electrosynthesis from Nitrate on Strained Ruthenium Nanoclusters. *J. Am. Chem. Soc.* **2020**, *142*, 7036-
508 7046.
- 509 (40) Wang, Y.; Li, H.; Zhou, W.; Zhang, X.; Zhang, B.; Yu, Y. Structurally Disordered RuO₂ Nanosheets
510 with Rich Oxygen Vacancies for Enhanced Nitrate Electroreduction to Ammonia. *Angew. Chem., Int. Ed.*
511 **2022**, *61*, e202202604.
- 512 (41) Yang, B.; Ding, W.; Zhang, H.; Zhang, S. Recent progress in electrochemical synthesis of ammonia
513 from nitrogen: strategies to improve the catalytic activity and selectivity. *Energy Environ. Sci.* **2021**, *14*,
514 672-687.
- 515 (42) Kim, C.; Song, J. Y.; Choi, C.; Ha, J. P.; Lee, W.; Nam, Y. T.; Lee, D. M.; Kim, G.; Gereige, I.; Jung,
516 W. B.; Lee, H.; Jung, Y.; Jeong, H.; Jung, H. T. Atomic-Scale Homogeneous RuCu Alloy Nanoparticles
517 for Highly Efficient Electrocatalytic Nitrogen Reduction. *Adv. Mater.* **2022**, *34*, e2205270.

518 For Table of Contents Only



519